INTERFACE

royalsocietypublishing.org/journal/rsif

Research



Cite this article: Nguyen DT, Smith AF, Jiménez JM. 2021 Stent strut streamlining and thickness reduction promote endothelialization. *J. R. Soc. Interface* **18**: 20210023. https://doi.org/10.1098/rsif.2021.0023

Received: 8 January 2021 Accepted: 22 July 2021

Subject Category:

Life Sciences-Engineering interface

Subject Areas:

biomedical engineering, bioengineering

Keywords:

stent, wound healing, shear stress, endothelialization, stent streamlining

Author for correspondence:

Juan M. Jiménez

e-mail: juanjimenez@umass.edu

Electronic supplementary material is available online at https://doi.org/10.6084/m9.figshare. c.5545136.

THE ROYAL SOCIETY

Stent strut streamlining and thickness reduction promote endothelialization

Duy T. Nguyen¹, Alexander F. Smith² and Juan M. Jiménez^{1,2}

¹Department of Mechanical and Industrial Engineering and ²Department of Biomedical Engineering, University of Massachusetts Amherst, Amherst, MA 01003, USA

DTN, 0000-0002-8293-2279; JMJ, 0000-0002-3915-2883

Stent thrombosis (ST) carries a high risk of myocardial infarction and death. Lack of endothelial coverage is an important prognostic indicator of ST after stenting. While stent strut thickness is a critical factor in ST, a mechanistic understanding of its effect is limited and the role of haemodynamics is unclear. Endothelialization was tested using a wound-healing assay and five different stent strut models ranging in height between 50 and 150 µm for circular arc (CA) and rectangular (RT) geometries and a control without struts. Under static conditions, all stent strut surfaces were completely endothelialized. Reversing pulsatile disturbed flow caused full endothelialization, except for the stent strut surfaces of the 100 and 150 µm RT geometries, while fully antegrade pulsatile undisturbed flow with a higher mean wall shear stress caused only the control and the $50 \mu m$ CA geometries to be fully endothelialized. Modest streamlining and decrease in height of the stent struts improved endothelial coverage of the peri-strut and stent strut surfaces in a haemodynamics dependent manner. This study highlights the impact of the stent strut height (thickness) and geometry (shape) on the local haemodynamics, modulating reendothelialization after stenting, an important factor in reducing the risk of stent thrombosis.

1. Introduction

Stent thrombosis (ST), although uncommon, remains a recognized complication of coronary stenting [1]. The formation of a thrombus within the stent, or immediately proximal or distal, can occur as early as during stent deployment to very late after deployment. The majority of cases occur after 1 year and can occur up to 7.3 years post stent implantation [2]. Mortality rates for ST have been recorded as high as 40% [3]. A separate study aiming to describe differences in treatment and in-hospital mortality observed higher mortality rates for early ST (7.9%) compared to late (3.8%) and very late ST (3.6%) [4]. Risk factors associated with ST include stent malapposition, neoatherosclerosis, inappropriate stent sizing, edge dissection, suboptimal stent deployment and uncovered stent struts [5,6]. Uncovered stent struts due to lack of endothelialization persist for 3-4 months in bare metal stent recipients, and up to 40 months after deployment for first-generation drug eluting stent (DES) recipients [7]. In comparison to first-generation DES, endothelial coverage is significantly increased in secondgeneration DES recipients at comparable time points post-stenting [8]. Lack of endothelial coverage in first-generation DES recipients proved to be the best predictor of ST, while lower incidence of ST with second-generation DES coincided with greater endothelialization rates [8,9]. The improved endothelialization rates and consequently lower incidence rates of ST with second-generation DES may be due to enhanced polymer biocompatibility, decreased drug concentrations, and thinner struts [10].

Given the importance of endothelial cell (EC) coverage in minimizing the risk of ST, various techniques have been used to accelerate endothelialization rates, including target site EC enrichment, gene expression manipulation and stent surface property modifications. *In vivo* studies have shown faster endothelialization rates when ECs loaded with biodegradable magnetic particles are

guided to the stented site with an external electromagnetic field [11]. Inhibition of the Rho-associated protein kinase (ROCK) also increased endothelialization rates both *in vivo* and *in vitro* [12]. The addition of micro-parallel grooves to the stent surface and alterations in the stent edge angle also accelerated endothelialization rates [13,14]. Other approaches have not been as successful. A functionalized stent using murine monoclonal antihuman CD34 antibodies and integrin-binding cyclic Arg-Gly-Asp peptides (cRGD) was designed to accelerate healing by recruiting circulating endothelial progenitor cells (EPCs) [15–17]. Although conceptually promising, a 1-year review of the TRIAS HR study showed EPC capture stents were inferior to DES in treating lesions with a high risk for restenosis [18].

In the absence of stents, EPCs could represent a source of cells for wound healing [19-22]. However, recent studies suggest that EPCs do not engraft the wounded blood vessel but may be indirectly regulating vascular repair via paracrine signalling [23]. By contrast, evidence exists suggesting that ECs at the edge of vascular wounds play a more direct role in wound healing. In a rat femoral artery, wound healing followed a two-step process where ECs from the edges first migrated toward the wound and then proliferated to completely cover the wound [24]. Similarly, resident ECs endothelialized the denuded pial artery of mice [25]. Endothelialization rates of a wound can vary, since endothelial migration and motility are sensitive to mechanical, chemical and biological stimuli. To test how biochemical signals affect wound healing, rats underwent carotid artery balloon catheter injuries and then systemic administration of basic fibroblast growth factor (FGF). Basic FGF significantly increased EC proliferation at the edge of the wound, and endothelial migration onto the wound with complete healing after 10 weeks [26]. Upon the routine use of stents in the catheterization laboratory, many wound-healing studies shifted to characterize the healing process of poststenting injuries instead of after balloon angioplasty. In wound-healing stenting studies, it was observed that ECs from the edges of the wound played a critical role in covering the injured site and the stent struts. In New Zealand white rabbits, the remnant endothelium adjacent to the stent struts completely covered the stented site 3 days post stent implantation in denuded iliac arteries [27]. Similar post-stenting results were observed in rabbit denuded iliac arteries, while vascular brachytherapy with γ-radiation significantly delayed the healing process [28]. By contrast, local delivery of vascular EGF via a catheter to the stented site accelerated endothelialization rates in a rabbit iliac artery injury model [29].

An important variable in endothelialization rates is the haemodynamic perturbations caused by the stent and its effect on the endothelium. In vitro, recirculation zones generated by a 400 μm high rectangular (RT) step, akin to stent strut haemodynamic perturbations, caused ECs to migrate away from high shear gradient regions, while uniform flow regions did not experience net migration [30]. In a pulsatile flow environment with a similar set-up, wound healing occurred faster in the uniform flow regions than in the reattachment zone of the recirculation zone next to the step [31]. In the work by Hsu et al., the faster cell migration rates coincided with the flow direction, while other experiments have observed that faster migration rates do not coincide with the predominant fluid flow direction [32,33]. Although these results correspond to thicknesses much greater than commercial stent struts, they highlight the

importance of understanding the effects of fluid flow on cell migration as it pertains to post-stenting wound healing and ST. Individual stent struts create recirculation zones and areas of low wall shear stress (WSS) in the peri-strut regions that may affect endothelialization rates [34-42]. In addition to the stent strut geometry, the local and bulk haemodynamics may be playing a role in endothelialization rates. Stented arterial sites experience pulsatile disturbed flow (DF) and/or undisturbed flow (UF), haemodynamic waveforms present in atherosusceptible and atheroprotective arterial sites, respectively [40]. We have demonstrated that under UF and DF, stent strut streamlining and decreased strut thickness mitigated the peri-strut recirculation zones and haemodynamic perturbations, concomitantly yielding a protective milieu via endothelial upregulation of the antithrombotic protein thrombomodulin and decreased fibrin deposition [34]. However, it is unclear how the local flow environment generated by different stent strut thicknesses and geometries affects EC migration and endothelialization.

To further understand endothelialization during wound healing following stent implantation, we investigated the effects of stent geometry and thickness on endothelialization. Endothelialization results are presented for *in vitro* stent strut models resembling commercial stents and streamlined versions varying in height under different flow conditions including DF, UF and static (S) conditions.

2. Material and methods

2.1. Stent strut model fabrication and cell seeding

Polydimethylsiloxane (PDMS) substrates were fabricated using custom-made moulds (Precision MicroFab, Severna Park, MD, USA) as described [34]. The mould geometries, circular arc (CA) or RT, were modelled using representative stent strut profiles with a constant width of 200 µm (figure 1a). The two CA geometries were 50 or 100 µm high, while the RT geometries were 50, 100 or 150 µm high. A blank PDMS substrate without struts served as a control geometry. The moulds were silanized with $20\,\mu l$ of (tridecafluoro-1,1,2,2-tetahydrooctyl)-1-trichlorosilane (United Chemical Technologies, Bristol, PA, USA) in a vacuum bell jar for 24 h at room temperature. After surface treatment, PDMS (SYLGAR 184, Dow, Midland, MI), mixed in a 1:10 curing agent to base ratio and degassed, was poured into the moulds and cured for 24 h at room temperature, 24 h at 45°C, 24 h in ethanol in an orbital shaker at room temperature and finally for 24 h at 45°C. The PDMS substrates were sterilized for $10\,s$ in 70% ethanol and 30 min in UV, and then coated with fibronectin (BD Biosciences, Bedford, MA) at a concentration of 0.1 mg ml⁻¹ in Hanks' balanced salt solution (Fisher Scientific, Pittsburgh, PA) for 24 h at room temperature, followed by seeding of human umbilical vein ECs (HUVECs; passage 3-10; Lonza, Basel, Switzerland) and cultured in complete EC growth medium-2 (EGM2; Lonza, Basel, Switzerland). Forty-eight hours after reaching confluence, the PDMS block that physically inhibited cell growth around either the stent strut or the flat control region was removed revealing a region void of cells to model the wound of a stented vessel (figure 1b,c).

2.2. Fluid flow system

The fluid flow system used in these experiments has been described before [34], only differing in the width of the parallel plate flow chamber (PPFC). Briefly, a specially designed PPFC generates a quasi-two-dimensional flow with a constant cross-section dimension of 1 mm in height and 57 mm in width.

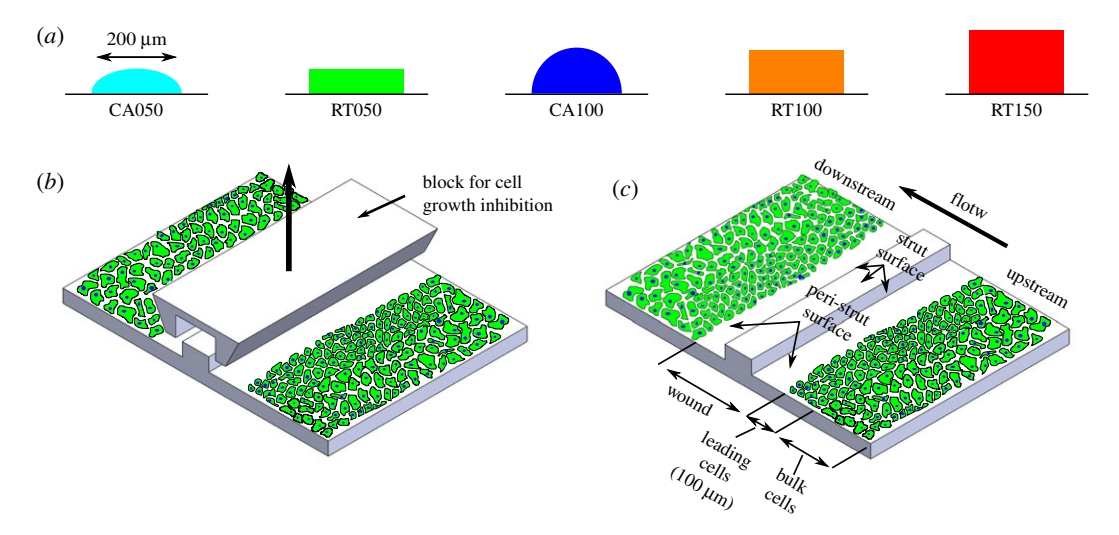


Figure 1. Five different stent strut geometries and a control without stent struts served as *in vitro* models for wound healing after stenting. (a) The geometries included a control, CA or RT stent strut with a constant width of 200 μ m and a height between 50 and 150 μ m. (b) A block was placed over each geometry before seeding with ECs and (c) removed 48 h after reaching confluence to generate an area void of ECs.

Given that the width to height ratio is much greater than 1, the flow in the spanwise direction does not change except near the side walls. Following boundary layer theory, cells are situated about 10 mm away from each side wall to avoid exposure to spanwise velocity gradients. The PPFC is equipped with plenum chambers to provide an even distribution of fluid flow when the flow enters the PPFC via the inlet or outlet during antegrade or retrograde portions of the waveforms, respectively. To allow the flow field to become more uniform, the cell medium enters the PPFC inlet and is diverted into two sideways streams that originate from the centre to fill the plenum and redirect the flow upwards and then horizontally toward the test section. These multiple turns allow for enhanced mixing and a more uniform flow field.

2.3. Live cell staining

Upon removal of the block that generated the wound, the ECs were incubated in Hoechst 33342 (Fisher Scientific, Pittsburgh, PA) at a 1.0 mg ml⁻¹ concentration in EGM2 serum-free cell medium for 30 min at 37°C, 5% CO₂ and 100% relative humidity. The cells were washed with warm phosphate-buffered saline solution and placed in the PPFC system, as described before, in 25 mM HEPES buffer concentration EGM2 cell medium [34].

2.4. Fluid flow waveforms

The PPFC was placed inside a constant temperature custom-made microscope environmental chamber at 37°C (In Vivo Scientific, St Louis, MO). The ECs were exposed to either pulsatile DF or UF waveforms, or S without flow as described before [34]. The flow rate at the inlet of the PPFC was monitored continuously with an ultrasonic flow meter (Transonic Systems, Inc., Ithaca, NY, USA).

2.5. Cell tracking

Cells were tracked using time-lapse brightfield and epifluorescence microscopy imaging every 30 min for up to 60 h. Cell tracking following experimental analysis was performed with Imaris software (Oxford Instruments, Abingdon, UK). Cell tracks were corroborated or rectified manually with ImageJ software.

2.6. Fluid flow quantities

The WSS experienced by the ECs was determined by measuring the volumetric flow rate at the inlet of the PPFC (Q_1) . Q_1 was

substituted into the incompressible continuity equation, $Q_1 = Q_2$, where subscript 1 denotes the plane where the volumetric flow rate is measured and subscript 2 is the plane of interest inside the PPFC where the ECs are located. Since the volumetric flow rate Q equals the average velocity (V) in a plane times the cross-sectional area (A) and the areas are known, the average or bulk velocity can be determined at the spanwise plane of interest where the ECs are located. After determining the average velocity for spanwise plane 2 from $V_2 = Q_1/A_2$, V_2 is substituted into the WSS relationship below to approximate the WSS experienced by the ECs. The WSS relationship is defined by

WSS =
$$\frac{3\mu V_2}{h/2} = \frac{3\mu Q_1/A_2}{h/2}$$
, (2.1)

where μ is the dynamic viscosity of EGM2 and h is the height inside the PPFC. Once the WSS is determined, the oscillatory shear index (OSI) can be calculated from

$$OSI = \frac{1}{2} \left(1 - \frac{\left| \int_0^T WSS \, dt \right|}{\int_0^T |WSS| \, dt} \right), \tag{2.2}$$

where *T* is the period of integration. A waveform with fully antegrade flow yields an OSI value of 0, while fully retrograde flow results in the OSI equal to 0.5.

2.7. Mean-squared displacement

In order to determine the movement of cells away from their original position at the beginning of each experiment, the mean-squared displacement (MSD) was determined with the following relationship:

$$MSD = \frac{1}{N-n} \sum_{k=1}^{N-n} (\mathbf{r}_{k+n} - \mathbf{r}_k)^2, \quad n = 1, \dots, N-1,$$
 (2.3)

where r is the position vector of each cell and can be written as $r_k = x_k i + y_k j$, and i and j are the side-to-side and top-to-bottom vectors in a Cartesian coordinate plane [43]. The variable k refers to a discrete time point and N - n is the total number of displacements. Equation (2.3) determines the MSD for all ECs in a defined region for discrete time points.

2.8. Cell segmentation for analyses

To assess the effect of relative cell location on endothelialization, the ECs on the upstream and downstream sides were divided into two regions (figure 1c). Each side had one region that

consisted of a 100 μm strip of ECs at the edge of the wound, and these cells were labelled leading cells. The second region for each side consisted of the remaining ECs outside of the 100 μm strip and were labelled bulk cells [44]. The upstream and downstream terms are also used for the static cases to differentiate the sides, although the static cases are not exposed to fluid flow.

2.9. Measurements and statistics

Three experiments were conducted for each geometry and fluid flow condition for a total of 54 different assessments. The average wound width generated by the PDMS block ranged between 651 and 799 µm as determined from the nuclear stain of cells along each side of the wound. The data from these experiments were used to determine the normalized peri-strut wound area and normalized stent wound area. The normalized peri-strut wound area is defined as the wound area excluding the stent surface divided by the wound area excluding the stent surface at time 0. Similarly, the normalized stent wound area is determined by dividing the stent surface wound area at any time point by the stent surface wound area at time 0. The average of the normalized peri-strut wound area and the normalized stent wound area are plotted along with the standard error of the mean to denote the variability as a function of the normalized time. The normalized time has a maximum value of 1 and is determined by dividing the time by the time when the wound is closed, or the 60 h time point when the experiment is finished. From the 54 wound-healing measurements, one representative case for each geometry and fluid flow condition was further analysed and the movement of every single cell was tracked for more than 60 h. The average number of cells analysed for each region of interest was about 1062 at time 0 and on average increased to 1248 by the end of the experiment primarily due to cells migrating into the regions of interest. The tracks generated from the motion of these cells were used for the remaining analyses. All statistical analyses were performed in Matlab software with custom scripts.

2.10. Directionality ratio

The angle of every EC displacement was determined and categorized as a downstream or upstream cell movement for the downstream bulk, downstream leading, upstream leading and upstream bulk regions (figure 1c). The directionality ratio is defined as the ratio of cells that move to close the wound versus those that do not. ECs on the downstream side migrate upstream to close the wound, whereas those on the upstream side migrate downstream to close the wound. A directionality ratio greater than 1 indicates that the majority of cells are migrating to close the wound, whereas a value less than 1 indicates cell migration away from the wound.

3. Results

3.1. Flow statistics

ECs away from the stent strut surface and peri-strut regions exposed to UF experienced a mean WSS value of 0.39 Pa with maximum and minimum WSS values of 0.54 and 0.23 Pa [45], respectively (figure 2). By contrast, ECs away from the stent strut surface and peri-strut regions exposed to DF experienced flow reversal that yielded a minimum WSS value of -0.11 Pa and a maximum of 0.19 Pa. The mean WSS for DF was 0.04 Pa. Although accelerating and decelerating, the UF waveform moved in the antegrade direction for the whole cycle yielding an OSI of 0, while the DF waveform reversed for a portion of the cycle resulting in an

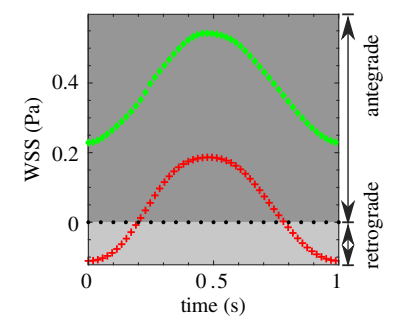


Figure 2. ECs experienced time-varying WSS when exposed to pulsatile disturbed (plus symbols) or undisturbed (filled diamonds) flow waveforms, and zero WSS under no flow static conditions (filled circles). The WSS values are affected by the stent surfaces yielding higher and lower local WSS values on the stent surfaces and the peri-strut regions, respectively [34].

OSI of 0.3. A similar flow field to that explored in this paper for the specific stent strut geometries and a similar flow chamber design, albeit narrower, was studied in depth by Jiménez *et al.* [34]. That study demonstrated that the peristrut and strut surfaces are affected by the stent strut geometry yielding higher WSS values on the surface of the stent struts and lower WSS values in the peri-strut regions when compared to WSS values away from the stent struts.

3.2. Fluid flow affects endothelial area coverage

To assess wound healing with various stent geometries, stent heights and flow conditions, the change in wound area was determined as a function of the normalized time. Figure 3 shows representative images at times 0 h and 60 h of the CA050 and RT100 cases for S, DF and UF conditions. Under static conditions, ECs successfully migrated to close the wound adjacent to the stent for both the RT and CA geometries and their respective heights ranging from 50 to $150 \, \mu m$ (figure 4a). Static conditions enabled endothelialization of not only the peri-strut area, but also of the stent strut surfaces independent of height and geometry with all struts covered (figure 4b).

While ECs migrated and covered the surface of all stent strut geometries under no flow, irrespective of the heights studied, static conditions are not representative of the in vivo pulsatile flow environment. Moreover, fluid flow plays a crucial role in EC mechanotransduction and migration biochemical pathways, and it would be expected to affect endothelialization [31,46,47]. In order to elucidate the role of fluid flow in wound healing and stent coverage, ECs were exposed to pulsatile DF and UF waveforms. The presence of flow affected endothelial coverage of both the peri-strut and stent surface areas. Under pulsatile DF, ECs successfully migrated to close the peri-strut wound on both the upstream and downstream sides of the stents, regardless of the strut geometry or height (figure 4a). However, the ECs failed to fully endothelialize the stent strut surfaces of the RT100 and RT150 geometries and 12-24% and 12-26% of the original wound remained unendothelialized, respectively, while the surface of the shorter RT050 stent strut was fully endothelialized (figure 4b, table 1). Increasing the height of the RT from 50 to 100 µm affected endothelial coverage of the strut surface and the RT100 strut did not completely endothelialize, while its streamlined counterpart, the

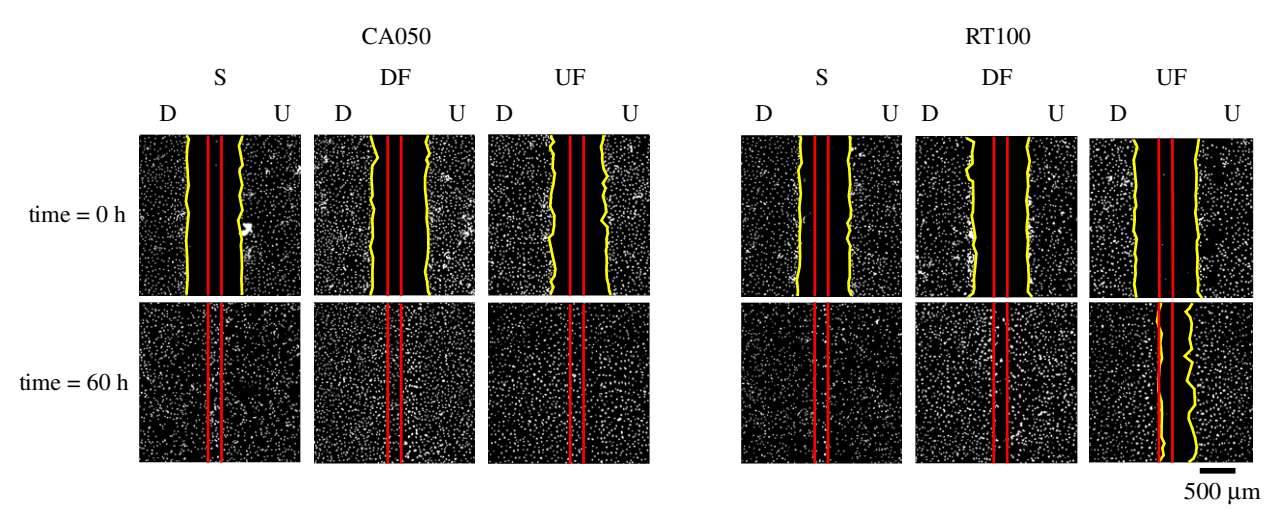


Figure 3. Representative wound-healing assay images of EC nuclei stain show the region of interest for the CA050 and RT100 at 0 and 60 h for the S, DF and UF cases, while red straight lines denote the edges of the stent, and yellow uneven curves correspond to the edge of the wound. The upstream region is denoted by U and the downstream region is denoted by D.

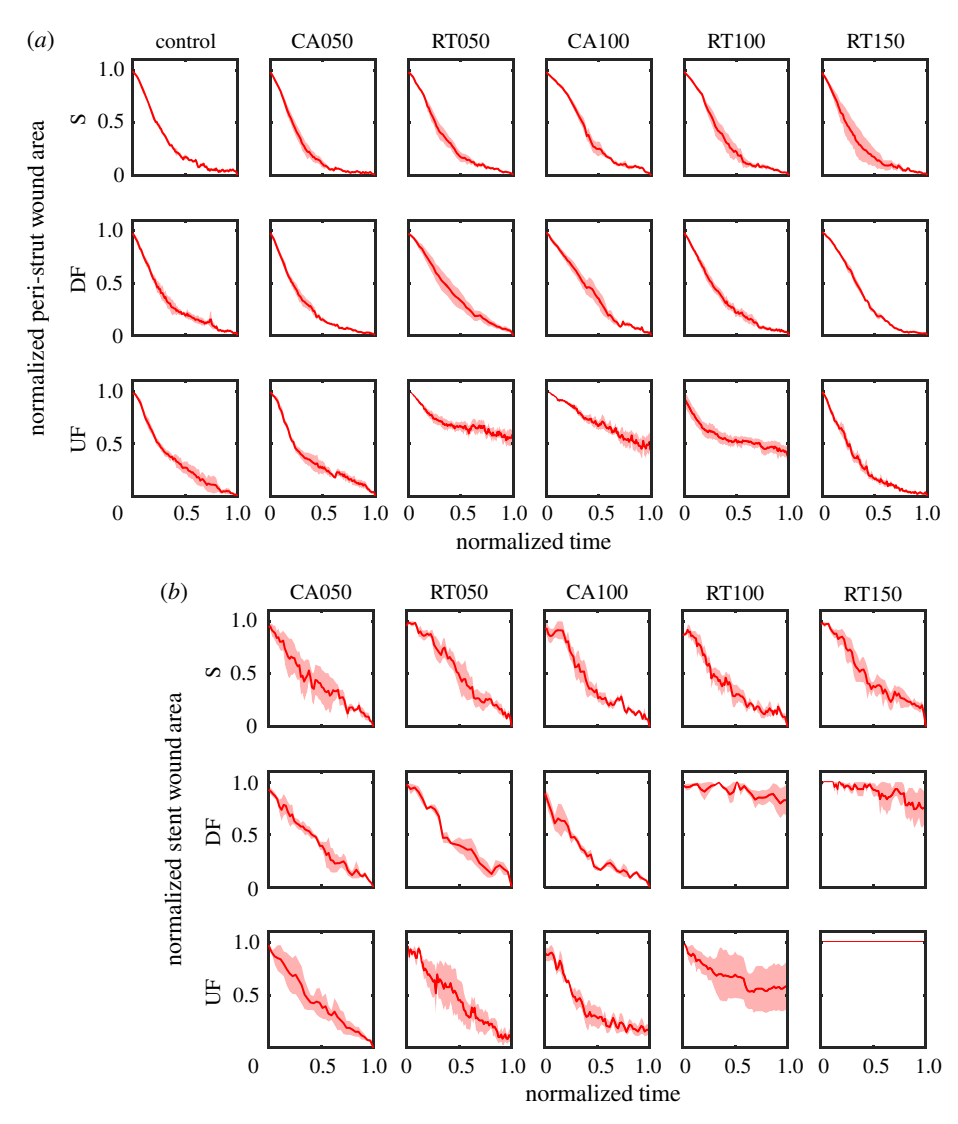


Figure 4. EC wound healing was tracked for the control, CA 50 and 100 μ m, and the RT 50, 100 and 150 μ m stent strut geometries under S, DF and UF. The normalized (*a*) peri-strut total wound area and (*b*) stent wound area for the control, CA050, RT050, CA100, RT100 and RT150 stent strut geometries under static, pulsatile DF and pulsatile UF. The shade around the curves denotes the error bars (n = 3).

CA100, completely rescued EC migration of the stent strut surface yielding 100% stent strut surface coverage (table 1).

The response of ECs to UF was more heterogeneous. Only the control and CA050 cases experienced full EC coverage for both the peri-strut and strut surface areas (figure 4). The peri-strut

and strut surface areas for the RT050, RT100 and CA100 did not fully endothelialize and 23–53%, 26–50% and 25–55% of the original wound remained unendothelialized, respectively (table 1). By contrast, the RT150 peri-strut area was fully endothelialized, while the stent strut surface did not endothelialize.

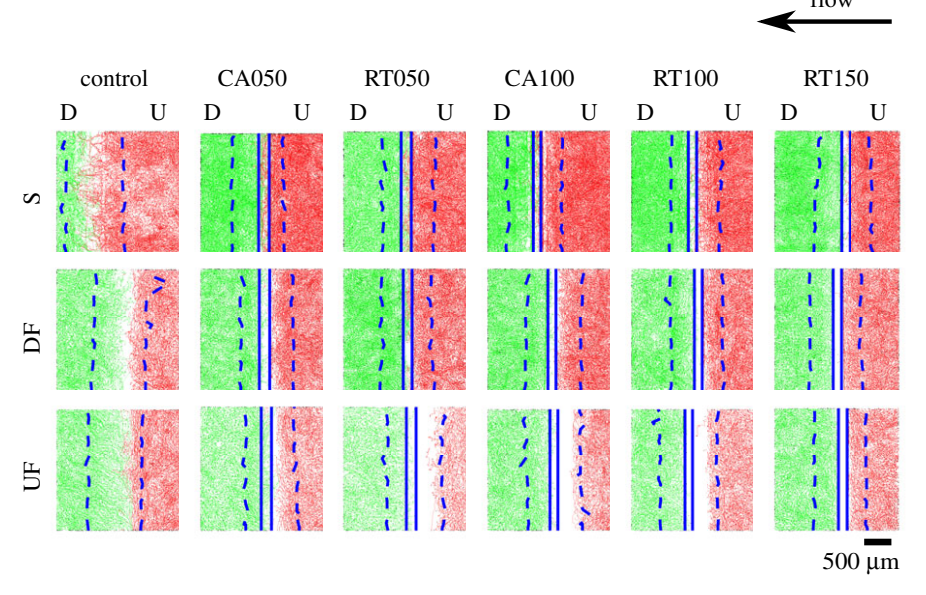


Figure 5. Migration tracks of all ECs at 60 h for the control, CA050, RT050, CA100, RT100 and RT150 geometry experiments under S, DF and UF conditions. Straight lines (—) denote the edges of the stent and uneven curves (- - -) correspond to the initial edges of the wound. The upstream and downstream regions are denoted by U and D, respectively. The tracks are coloured according to the coordinate of their first time point with green and red tracks originating on the downstream and upstream side of the wound, respectively.

Table 1. Wound size range of the EC migration assay at normalized time 1. A value of 0 denotes complete coverage of the wound and successful EC migration, while a value of 1 denotes the initial wound size (n = 3).

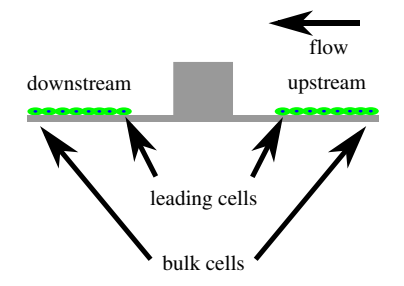
	control	CA050	RT050	CA100	RT100	RT150
S	0	0	0	0	0	0
DF	0	0	0	0	0.12-0.24	0.12-0.26
UF	0	0	0.23-0.53	0.26-0.50	0.25-0.55	0.24-0.30

The complexity of endothelialization of the peri-strut and strut surfaces is highlighted in figure 5, showing the individual track for each EC over a 60 h period, the edge of the original wound and the edge of the stent strut where applicable. For the static cases, the wounds are completely covered by ECs even if the strut surfaces do not seem 100% confluent, since the EC tracks only show the trajectory of the EC centroid and not of the whole-cell cross-sectional area. This is especially noticeable on the stent strut surfaces, since fewer cells have travelled the strut surfaces given that this is the last area that tends to get endothelialized. For the static condition, there is no preferred side from which the cells predominantly close the wound. In some cases, migration was dominated by the downstream side ECs, while in other cases by upstream side ECs. However, exposure to pulsatile fluid flow altered the ratio of ECs that covered the wound. Exposure to DF clearly affected the wound-healing process, since most cells that covered the wound originated from the downstream side and migrated upstream against the predominant fluid flow direction. The percentage of cells that originated from the downstream side and covered the wound for the DF cases ranged between 51 and 81 per cent. The ratio was further changed when exposed to UF. The percentage of ECs from the downstream side that covered the wound increased to a range between 64 and 96 per cent. Exposure to UF caused downstream ECs to cover the peri-strut wound area of all geometries, while the upstream side was only covered for the control, CA050 and RT150 geometries by upstream ECs.

3.3. Cells at the edge of the wound lead endothelialization

The individual and average velocity of the leading and bulk ECs was determined for the upstream and downstream sides of all geometries and flow conditions (figure 6; electronic supplementary material, figure S1). For the static condition, the downstream and upstream bulk ECs for all geometries reached a maximum mean velocity of 7.6 ± 0.54 and $7.1 \pm$ 0.92 nm s⁻¹, respectively, around 12 h and the mean velocity remained relatively constant, between 6.1 and 7.6 nm s after the initial 12 h. Exposure to both DF and UF also prompted the bulk ECs to accelerate continuously until about 12 h where a maximum mean velocity range between 4.6 and 5.5 nm s⁻¹ was observed between both the downstream and upstream sides. In contrast with the static cases where the bulk EC velocities tended to remain relatively constant after 12 h, the migratory velocity of bulk ECs exposed to flow decreased monotonically with time after reaching a maximum velocity around 12 h.

Similar to the bulk ECs, under static conditions, the leading ECs for the downstream and upstream sides also reached maximum mean velocities, 8.9 ± 2.6 and 8.7 ± 1.9 nm s⁻¹, around 12 h respectively. Leading ECs tended to migrate



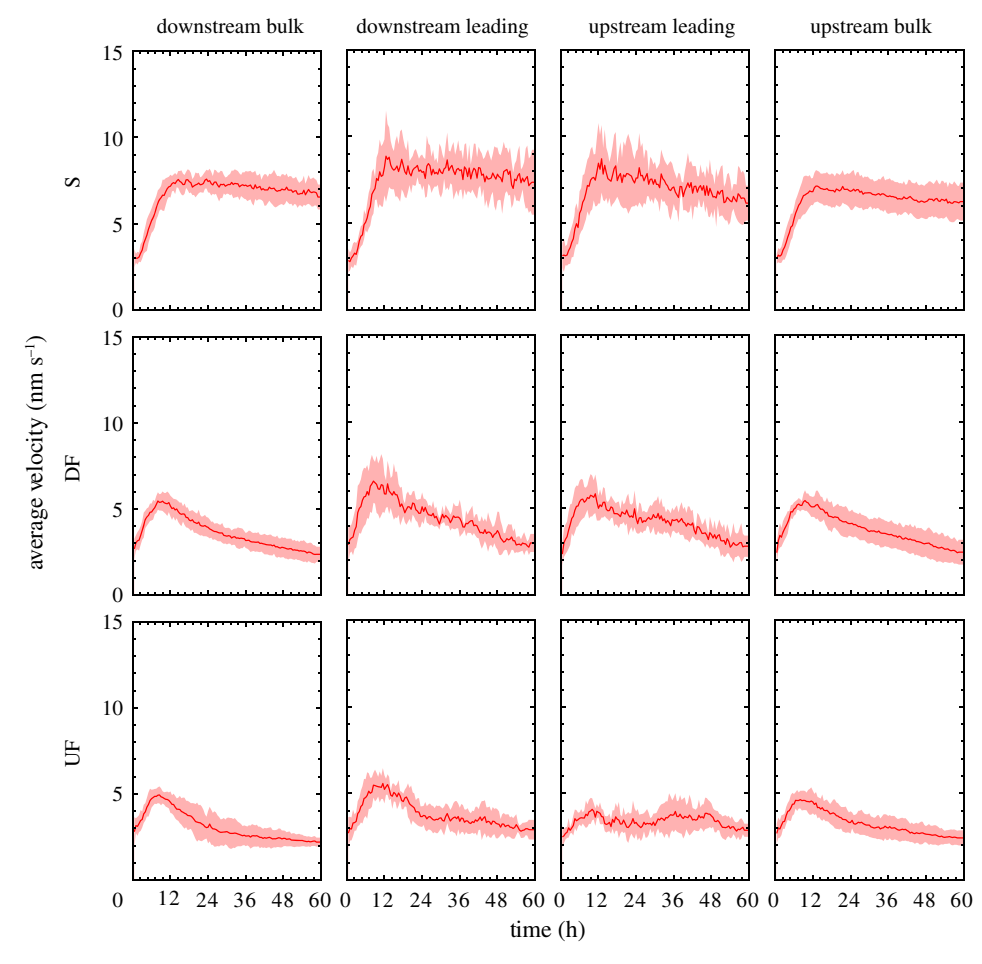


Figure 6. The migration velocities (solid curve) and one standard deviation (shaded area) corresponding to the average velocity of all ECs for the control, CA050, RT050, CA100, RT100 and RT150 geometries under S, DF and UF conditions. The average velocities for all geometries are plotted separately for the leading and bulk cells on the downstream and upstream sides.

with higher velocities than their bulk counterparts under static conditions. After reaching a maximum velocity around 12 h, the leading EC mean velocities for all static cases fluctuated about relatively constant mean velocities. For the DF case, the leading cells accelerated until approximately 12 h and reached a maximum of about 8.9 nm s⁻¹ and 8.7 nm s⁻¹ for the downstream and upstream sides, respectively, and started to decelerate thereafter. A similar trend was observed for the downstream side of all geometries when ECs were exposed to UF. However, on the upstream side where the ECs failed to close the wound for several of the geometries when exposed to UF, the velocity curves for the leading EC velocities show a highly attenuated acceleration phase and velocity peak, which differed from the other cases. When exposed to UF, the velocity of the leading ECs on the upstream side ranged between 1.3 and 6.1 nm s⁻¹, which is much lower than the average velocity for all other flow conditions.

3.4. Depressed mean-squared displacement values of leading cells reflect lack of endothelialization

The MSD and cell track distributions of the bulk and leading ECs for the upstream and downstream sides were determined separately to identify the predominant ECs involved in wound healing (figure 7; electronic supplementary material, figure S2). For the static cases, the MSD values at 60 h were greater for the leading ECs and ranged between 0.20 and 0.39 mm², while the bulk EC MSD values ranged between 0.10 and 0.21 mm². Exposing the ECs to DF caused an overall decrease in MSD values for all geometries. In comparison to the leading cells for the static cases, the effects of DF were more dramatically observed in the leading cells where MSD values decreased on average by 82.62% and 75.39% on the downstream and upstream sides, respectively, while the overall trends remained similar to the static conditions where MSD values at 60 h were greater for leading than bulk ECs.

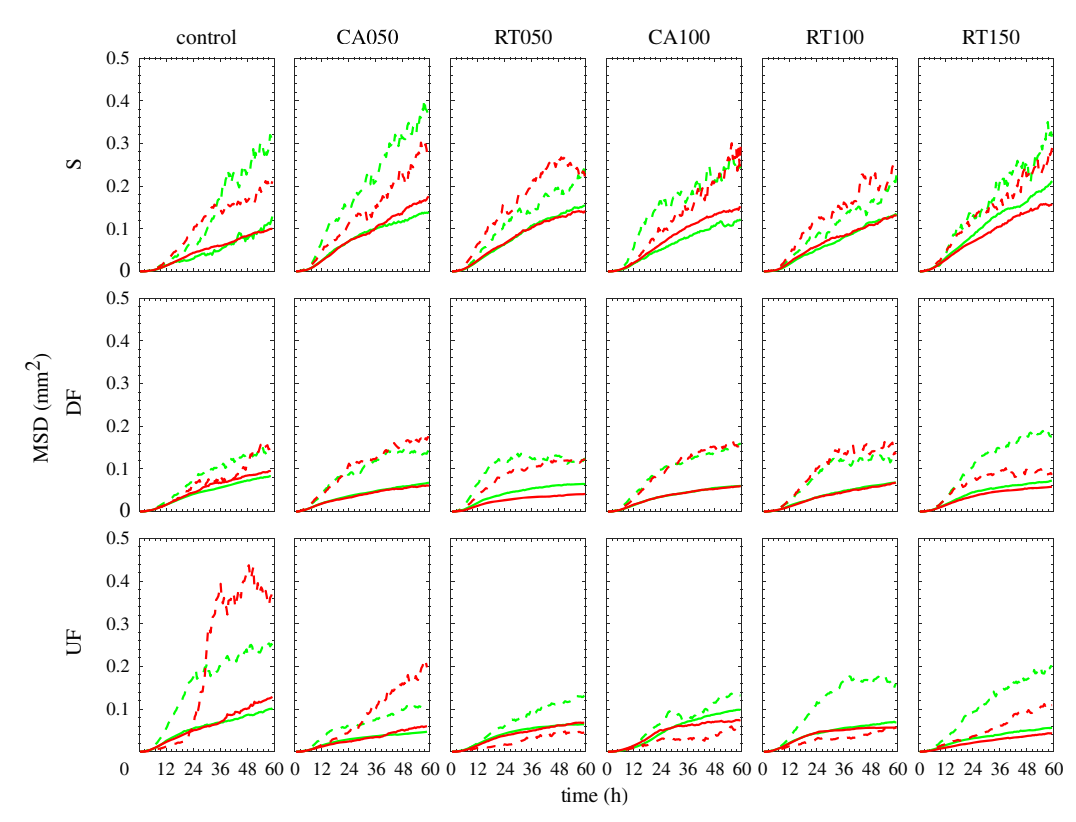


Figure 7. Average MSD of leading upstream (- - -), leading downstream (- - -), bulk upstream (—) and bulk downstream (—) ECs for the duration of the control, CA050, RT050, CA100, RT100 and RT150 geometry experiments under S, DF and UF conditions. The tracks are coloured according to the coordinate of their first time point with green and red tracks originating on the downstream and upstream side of the wound, respectively.

Exposing ECs to UF affected the leading and bulk ECs differently. The bulk EC MSD values for UF ranged between 0.04 and 0.13 mm² and were similar to the DF MSD values. By contrast, the leading EC MSD values differed depending on the final endothelial coverage of the wound. For the control and CA050 UF cases where complete endothelialization of the peri-strut and stent surfaces was attained, the MSD values for both the upstream and downstream leading ECs ranged between 0.12 and 0.43 mm² and were greater than the bulk EC MSD values that ranged between 0.04 and 0.13 mm² at 60 h. Except for the stent strut surface, the RT150 experienced complete endothelialization of the peri-strut area on both the downstream and upstream sides and yielded leading EC MSD values between 0.11 and 0.19 mm² at 60 h, which were greater than the bulk EC MSD values. The downstream peristrut sides of the RT050, RT100 and CA100 were completely endothelialized and the leading EC MSD values ranged between 0.13 and 0.18 mm² at 60 h and were greater than the upstream and downstream side bulk EC MSD values. By contrast, the ECs on the upstream side of the RT050, RT100 and CA100 did not cover the wound and displayed different leading EC MSD value from cases where endothelial coverage was attained. The EC MSD values for the leading ECs on the upstream side of the RT050, RT100 and CA100 ranged between 0.05 and 0.06 mm² at 60 h, and in contrast with the other cases, the leading EC MSD values were lower than the upstream and downstream bulk EC MSD values.

3.5. Directionality ratio influences wound closure

The directionality ratio was determined from the direction angle of all EC displacements (electronic supplementary material, figures S3 and S4). Table 2 shows the directionality ratio for the downstream bulk, downstream leading, upstream

leading and upstream bulk regions. For all static cases, the leading and bulk ECs for the upstream and downstream side had directionality ratios greater than 1 indicating that the majority of EC displacements were in the direction of closing the wound. For the static cases, the leading cells had larger directionality ratios ranging between 1.26 and 2.66, while the bulk EC directionality ratios ranged between 1.19 and 1.6. Similar results were observed for DF, except that the directionality ratio for the downstream leading ECs increased for all geometries and ranged between 1.94 and 3.25. However, no appreciable differences in directionality ratios were observed between the downstream and upstream bulk ECs of the S and DF cases. By contrast, when the ECs were exposed to UF, the directionality ratios showed a stronger dependence on stent strut geometry. For the control geometry, UF affected both the downstream bulk and leading EC directionality ratios reaching values between 2.84 and 5.90, which compensated for the wound opening directionality ratios on the upstream side, which are less than 1. Directionality ratio increases were prevalent for the downstream leading ECs in the peri-strut region of all stent strut geometries and ranged between 2.55 and 2.9. Under UF, the CA050 and RT150 were the only cases where the EC directionality ratio was greater than 1 for both the upstream leading and bulk cells. The upstream bulk EC directionality ratios for the RT050, CA100 and RT100 were less than 1. The upstream leading EC directionality ratios of the RT050 and RT100 were close to 1, while it was much lower than 1 for the CA100 geometry.

3.6. Temporal migration directionality affects wound healing

Figure 8 shows EC migration directionality for all geometries and flow conditions with respect to time. The angle of each

Table 2. Directionality ratio for the downstream bulk, downstream leading, upstream leading and upstream bulk cell regions. The directionality ratio is defined as the ratio of cells that move to close the wound versus those that do not. Directionality ratios greater than 1 correspond to cellular displacements in the direction of closing the wound and directionality ratios less than 1 correspond to cellular displacements in the direction of opening the wound. The directionality ratio was calculated for leading cells, defined as cells within 100 μm of the edge of the wound, and bulk cells, defined as the remainder of ECs in the wound, for both the downstream and upstream regions of the stent strut.

flow	geometry	downstream bulk	downstream leading	upstream leading	upstream bulk
S	control	1.19	1.26	2.66	1.24
	CA050	1.34	1.94	1.59	1.39
	RT050	1.47	1.71	1.73	1.51
	CA100	1.20	1.81	1.81	1.17
	RT100	1.24	1.69	1.70	1.37
	RT150	1.60	1.93	2.07	1.49
DF	control	1.86	3.25	1.43	1.02
	CA050	1.80	2.26	2.08	1.37
	RT050	1.65	2.15	2.22	1.28
	CA100	1.59	2.19	2.35	1.30
	RT100	1.38	1.94	1.56	1.07
	RT150	1.44	2.18	1.95	1.17
UF	control	2.84	5.90	0.72	0.92
	CA050	1.54	2.62	1.90	1.22
	RT050	2.16	2.70	1.02	0.80
	CA100	2.08	2.90	0.65	0.77
	RT100	1.86	2.87	1.10	0.95
	RT150	1.37	2.55	2.46	1.14

cell movement was grouped into one of four migration directionality quadrants, as follows: left ($\geq 135^{\circ}$ and $< 225^{\circ}$), up ($\geq 45^{\circ}$ and $< 135^{\circ}$), right ($\geq 315^{\circ}$ and $< 45^{\circ}$) and down ($\geq 225^{\circ}$ and $< 315^{\circ}$). For static conditions, the migration directionality for bulk ECs was approximately equal in all directions, but with a limited preference toward closing the wound with more downstream and upstream bulk ECs moving toward the right and left, respectively (figure 8a). Averaging for all geometries shows that 30.16% of cells in the downstream bulk migrated to close the wound, with a similar percentage of cells observed for those on the upstream side (30.3%).

This trend was also observed when ECs were exposed to pulsatile DF, where 34.3% and 27.2% of bulk ECs migrated to close the wound on the downstream and upstream sides, respectively. During the initial 12 h, where cell speeds were observed to be the highest, a maximum of 48% of bulk ECs migrated to close the wound. After the initial 12 h, preferred migration directionality to close the wound was lost and the ECs adopted a random migration pattern with all four directions experiencing nearly 25% migration directionality. Exposure to pulsatile UF elicited the most pronounced migration directionality difference in the four quadrants. The migration directionality for downstream bulk ECs peaked at 64% during the initial 12 h, where these cells migrated upstream against the flow direction to close the wound. By contrast, only 48.8% of bulk ECs on the upstream side migrated with the flow direction to close the wound during the peak response of the initial 12 h.

The migration directionality values for the leading ECs on both the downstream and upstream sides for static conditions

corresponded to a migratory phenotype for closing the wound (figure 8b). On the downstream side, the migration directionality values peaked at 78.8% during the initial 12 h. ECs on the upstream side migrated with similar proportions, where 77.8% of cells migrated to close the wound. Similar to the static results, the addition of DF elicited a wound closing phenotype in the leading ECs for both the upstream and downstream side. During peak EC migration directionality, 75.1% and 75.5% of ECs migrated to close the wound on the downstream and upstream sides, respectively. When exposed to UF, the leading ECs for all stent geometries preferentially migrated against the direction of flow. On the downstream side, a maximum of 91.23% of leading ECs migrated against the direction of flow during the initial 12 h. Interestingly, only 70.4% of ECs migrated to close the wound on the upstream side during the peak response. However, the maximum migration directionality corresponded to the CA050 geometry, which was endothelialized. For the RT050, RT100 and CA100, which did not experience upstream peri-strut EC coverage, the migration directionality for the upstream side was at most 50.5% for the left direction.

4. Discussion

Post-mortem studies from late DES thrombosis observed partial arterial healing with fibrin deposition and incomplete reendothelialization [7,48–50]. Subsequently, endothelial coverage was identified as the dominant histological predictor of in-ST [9]. Since the endothelium regulates blood coagulation

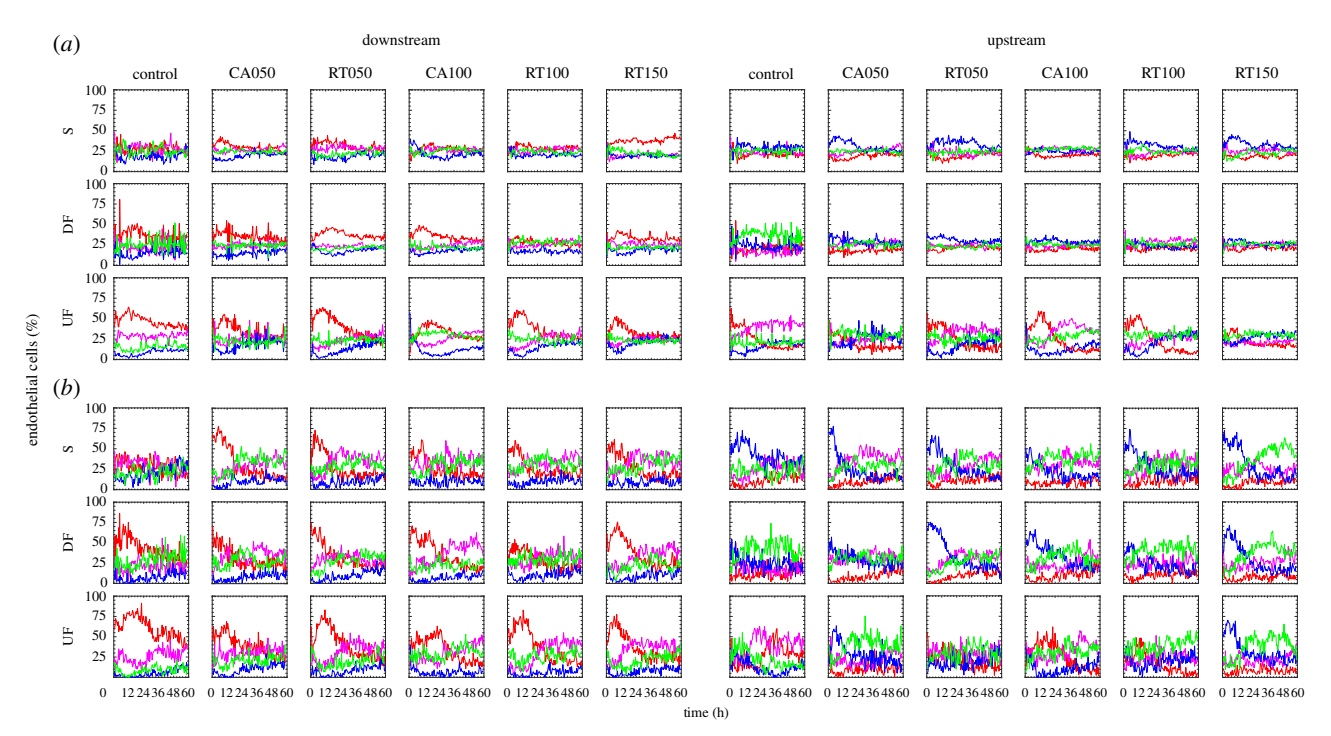


Figure 8. EC migration directionality as a function of time for ECs within the (a) bulk and (b) leading regions of the wound ECs for the duration of the control, CA050, RT050, CA100, RT100 and RT150 geometry experiments under S, DF and UF conditions. The percentage of cells moving right (red), left (blue), up (magenta) or down (green) is defined by four equal quadrants between 0 and 360°. The directionality quadrants are defined as follows: left (≥135° and <225°), up (≥45° and <135°), right (≥315° and <45°) and down (≥225° and <315°). Random cell migration directionality is depicted by 25% of cells moving in each direction. Bulk fluid flow direction is from right to left.

by acting as a physical barrier between blood and the highly thrombogenic extracellular matrix, removal of the endothelium by stenting increases the risk of in-ST [9,51-53]. Studies have identified stent design variables, such as polymer coatings, drugs, drug release kinetics and strut thickness that affect reendothelialization [54-57]. Although the understanding that thicker stent strut dimensions are associated with a greater risk of thrombosis, a mechanism for how flow and the stent strut thickness and geometry affect endothelialization has not been established [58]. Modest streamlining and strut thickness reduction of stent struts significantly modify the peri-strut haemodynamic environment conferring an anti-thrombotic peri-strut milieu [34,35]. Stent strut streamlining and thickness reduction decreased the size and velocity of peri-strut fluid recirculation zones, minimized fibrin deposition and yielded a local antithrombotic endothelial phenotype on an intact endothelial monolayer [34]. Although encouraging, these previous endothelial results are only relevant for an intact endothelial monolayer, whereas the lack of endothelium (lack of reendothelialization) is the major predictor of in-stent thrombosis. Our studies herein demonstrate that the stent strut geometry and height regulate reendothelialization of the peri-strut and strut surface environments (figure 9).

In the absence of flow, ECs successfully covered all stent strut surfaces regardless of the stent geometry or height, which varied from gradual varying slopes for the CAs to steeper slopes for the walls of the RT struts and heights that ranged from 50 to 150 µm. These results highlighted that stent geometry and thickness are not intrinsically the impeding factors in reendothelialization but play a synergistic role with other factors including haemodynamics. Our present study and a previous report [59] reveal that haemodynamics play an important role in endothelialization. *In vitro* steady

flow experiments with RT shapes resembling simple stent strut models ranging in height from 25 to 250 µm showed that surface endothelialization was inversely proportional to the height with a significant decrease of endothelial coverage occurring at 100 µm thicknesses and above [59]. Another *in vitro* study demonstrated that changing the geometry by decreasing the slope of the side walls of stent strut models from 90° to 35° increased rates of endothelialization [14]. While our results agree with the significance of the stent strut thickness and side wall slope (geometry), these stent strut design variables do not simply dictate endothelialization; instead the synergy between fluid flow and stent strut thickness and geometry have an impact.

ECs were exposed to DF to recapitulate the haemodynamics at bifurcations and arterial sites that experience temporal retrograde flow [60]. During DF, the net flow direction reverses for a portion of the cycle and the larger and smaller peri-strut recirculation zones alternate sides, exposing ECs in the peri-strut region to growing and shrinking recirculation zones and reversing flow direction [34,35]. In contrast with the static conditions, the final endothelial area coverage mirrored the trends of the average recirculation zone sizes. In general, endothelialization decreased as the thickness increased and the level of streamlining decreased, both physical stent strut parameters that have been shown to cause an increase in the average recirculation zone size [34,35]. Nevertheless, under UF, the control and CA050 experienced no recirculation zones and were fully endothelialized. In general, ECs exposed to pulsatile UF achieved inferior area coverage compared to their DF stent strut counterpart, except for the streamlined CA050 strut and the control. This was surprising given that DF has been shown to disrupt EC alignment and cell polarization [61,62]. EC polarization is crucial for directed cell migration and involves reorganization of the actin

	downstream	stent strut surface	upstream	
s	control RT050 CA050 RT100 CA100 RT150	CA050 RT100 CA100 RT150	control RT050 CA050 RT100 CA100 RT150	
DF	control RT050 CA050 RT100 CA100 RT150	CA050 CA100	control RT050 CA050 RT100 CA100 RT150	
UF	control RT050 CA050 RT100 CA100 RT150	CA050	CA050 RT150	

Figure 9. Endothelial coverage of the stent strut surface and the downstream and upstream peri-strut regions is affected by the local haemodynamic forces created by the different geometries. Completely endothelialized geometries are depicted under different conditions. Under S conditions, all geometries are fully endothelialized, including the peri-strut environments and the stent surfaces. For DF both the upstream and downstream peri-strut regions are fully endothelialized for all geometries, while only the control, CA050, CA100 and RT050 experienced full endothelial coverage. For UF, the downstream peri-strut region of all geometries was fully endothelialized, while just the control and CA050 experienced full endothelial coverage. The upstream peri-strut region of the RT150 was fully endothelialized. The downstream peri-strut environment is fully endothelialized for all geometries regardless of the fluid flow conditions. Modest streamlining and strut thinning support endothelial coverage for all flow conditions, similar to the control case without a stent strut.

cytoskeleton, organelles and microtubules to orient the cell in the direction of migration and local activation of GTPases RhoA, Rac and Cdc42 for protrusion formation of the polarizing cell [63,64]. The GTPase RhoA, which can be activated by steady shear stress, is instrumental in directed cell migration and regulates the formation of actin stress fibres and focal adhesions in cell migration [65,66]. In *in vitro* and *in vivo* stent environments, the inhibition of ROCK increased cell migration and improved wound healing, highlighting the complex relationship between the local flow field caused by the stents and their effect on the endothelial migratory phenotype [12,66].

In the cases where UF EC area coverage was inferior to that of DF, ECs on the upstream side of the stent strut contributed very little to the closing of the wound or simply migrated against the direction of flow and away from the wound. The change in a migratory direction clearly affected wound closure. EC migration direction reports vary widely in the literature. Wound-healing studies with ECs seeded only on the upstream side of $100 \, \mu m$ RT stent strut models showed that ECs migrated in the direction of the flow when exposed to steady flow and with greater deviation in migration direction from the predominant flow axis when exposed to oscillatory flow with not net flow [12]. Although there are similarities with our experiments, the results may differ due to the absence of ECs on the downstream side of the stent struts and basic differences in the waveforms, such as lack of pulsatile flow for the higher shear rate waveform and no net flow for the oscillatory waveform. Under steady flow and in an intact endothelial monolayer, ECs downstream of 400 µm-thick RT steps migrated predominantly in the

direction of the flow away from the reattachment point where the cells experienced the highest spatial WSS gradients [30,67]. Even though in our experiments the recirculation zones on the upstream side of the stent struts vary in size throughout the pulsatile cycle, it is unlikely that the temporal WSS gradient played a role in the upstream cells migrating against the flow, since the recirculation zone dimensions are much smaller and likely only affect cells very near the stent strut. More importantly the effect of upstream ECs migrating against the flow was observed, albeit to a much lesser degree, in the CA050 and the control, which experienced no spatial WSS gradient. In a wound-healing pulsatile, UF experiment without physical perturbations like stents, cells preferably migrated from the upstream side in the direction of the flow, while uniform EC migration was observed from the upstream and downstream edges for static and DF conditions [31]. The differences in cell migration direction also extend to in vivo experiments. Following an injury in the middle cerebral artery of mice, ECs primarily migrated downstream from the proximal side of the wound in the direction of flow [25]. By contrast, during mouse embryonic development, ECs within growing vessels migrated against the direction of blood flow [68].

Despite failed migration from ECs on the upstream side of the RT050, CA100 and RT100 when exposed to UF, the RT050, CA100 and RT100 still achieved stent surface coverage albeit from downstream ECs. This coverage from downstream ECs highlights the varying role that different EC subpopulations can play in the endothelialization process under different haemodynamic conditions. When comparing MSD values of leading versus bulk cells, leading cells with higher overall

MSD values result in peri-strut endothelial coverage and lower leading cell MSD values correspond to failed endothelialization of the wound. The importance of leading cells in wound healing after stenting is not fully understood, but in the absence of a stent, it is known that leading cells at or near the edge of a wound tend to display a different phenotype than the remaining bulk cells away from the wound. Leading cells display localization of collective cell migration molecules Rac, integrin β 1 and PI3 K, while bulk cells do not and inhibition of these molecules disrupts collective cell migration [69]. Inhibition of ROCK converts most edge cells to leading cells, while transfection with constitutively active RhoA abrogates the transformation of edge cells to leading cells emphasizing the control played by ROCK in the dynamic distribution and activity of actin filament bundles, myosin II and microtubules [70]. Leading cells experience heightened production of reactive oxygen species (ROS), which modulate actin cytoskeleton reorganization necessary for migration, while ROS inhibition retards EC migration [71]. ECs under UF experience lower ROS production [72] potentially affecting endothelialization in the context of stenting although it does not completely explain the differences observed herein for the different strut geometries when exposed to UF. The role of leading cells in stent endothelialization under different waveforms needs to be explored further.

In wound-healing experiments where ECs experienced either static, low steady WSS or high steady WSS, the highest cell migration velocity was observed with static and upstream leading edge cells that predominantly migrated in the direction of the high WSS flow [73]. This contrasts with our experiments where exposure to pulsatile DF and UF consistently resulted in declining cell speeds across all stent geometries and the control. Under static conditions, the average speed remained persistent, while ECs experiencing pulsatile DF and UF decelerate monotonically, after reaching peak migration velocities (electronic supplementary material, figure S1).

Although *in vitro* work has been instrumental in elucidating the role of mechanical forces in biochemical pathways, potential limitations in our study are primarily related to the *in vitro* nature of the work. The cells are grown in a two-dimensional environment lacking the three-dimensional nature of a blood vessel. The material composition of the blood and the blood vessel are primarily absent from the cell medium and the substrate where the cells are grown, respectively. Stents are deployed in heterogeneous atherosclerotic environments that can affect wound healing and

are absent from these studies. Although the focus of this study was the effect of the local flow field generated by the different stent strut geometries on cell migration, the inclusion of some of these in vivo variables can provide a more accurate wound-healing response. Cells are cultured in static conditions until the onset of the different waveforms. Although the experiments lasted for a minimum of 60 h, it is possible that the sudden onset of flow affected the cell phenotype [74]. Image acquisition was limited to 30 min intervals to decrease photobleaching, which limits observation of apoptotic and mitotic events that could contribute to the cell population in an experiment. The sizes of the wounds were determined by the nuclear position within each cell and not by the cell membrane potentially overestimating the size of the wounds and making them seem less uniform and more variable than the true wound dimensions. Although the flow rate was measured at the inlet of the PPFC to determine the WSS, without an actual measurement of the velocity gradients inside the PPFC, the assumption of a Hagen-Poiseuille velocity profile may yield lower WSS values than those experienced by the cells.

To the best of our knowledge, this is the first study that highlights the effects of streamlining and thinning of stent strut models on EC migration under pulsatile DF and UF waveforms, shedding light on the complicated factors affecting endothelialization in the context of stent struts. These results are relevant in the design of stents to promote reendothelialization of stented regions, reduce the likelihood of late ST and improve clinical outcomes. The underlying haemodynamic and biomolecular mechanisms that dictate cell persistent migration speeds and direction, especially in the context of stenting, remain unclear and need to be explored further.

Data accessibility. Additional data are provided in the electronic supplementary material.

Authors' contributions. J.M.J. conceived, designed and conducted the experiments. D.T.N. and A.F.S. tracked the cell movements. D.T.N. and J.M.J. analysed and interpreted the data. D.T.N., A.F.S. and J.M.J. helped draft the manuscript. All authors gave final approval for publication.

Competing interests. We declare we have no competing interests.

Funding. This work was supported by the National Heart, Lung, and Blood Institute (NHLBI) grant no. K25 HL107617 and NSF grant no. CAREER CMMI1842308 (to J.M.J.), and Graduate Research Fellowship Program S12100000000937 (to A.F.S.).

Acknowledgements. We thank Dr Melissa D. Sánchez for constructive criticism.

References

- Reejhsinghani R, Lotfi A. 2015 Prevention of stent thrombosis: challenges and solutions. Vasc. Health Risk Manag. 11, 93. (doi:10.2147/vhrm.s43357)
- Waksman R et al. 2014 Correlates and outcomes of late and very late drug-eluting stent thrombosis. JACC Cardiovasc. Interv. 7, 1093—1102. (doi:10.1016/j.jcin. 2014.04.017)
- Holmes DR, Kereiakes DJ, Garg S, Serruys PW, Dehmer GJ, Ellis SG, Williams DO, Kimura T, Moliterno DJ. 2010 Stent thrombosis. J. Am. Coll. Cardiol. 56, 1357–1365. (doi:10.1016/j.jacc.2010.07. 016)
- Armstrong EJ et al. 2012 Clinical presentation, management, and outcomes of angiographically documented early, late, and very late stent thrombosis. JACC Cardiovasc. Interv. 5, 131–140. (doi:10.1016/j.jcin.2011.10.013)
- Prati F et al. 2015 Suboptimal stent deployment is associated with subacute stent thrombosis: optical coherence tomography insights from a multicenter matched study. From the CLI Foundation investigators: the CLI-THRO study. Am. Heart J. 169, 249–256. (doi:10.1016/j.ahj.2014.11. 012)
- Souteyrand G et al. 2016 Mechanisms of stent thrombosis analysed by optical coherence tomography: insights from the national PESTO French registry. Eur. Heart J. 37, 1208–1216. (doi:10.1093/eurheartj/ ehv711)
- Joner M et al. 2006 Pathology of drug-eluting stents in humans. J. Am. Coll. Cardiol. 48, 193–202. (doi:10.1016/j.jacc.2006.03.042)
- Otsuka F et al. 2014 Pathology of second-generation everolimus-eluting stents versus first-generation sirolimus-and paclitaxel-eluting stents in humans.

Circulation **129**, 211–223. (doi:10.1161/CIRCULATIONAHA.113.001790)

- Finn AV, Joner M, Nakazawa G, Kolodgie F, Newell J, John MC, Gold HK, Virmani R. 2007 Pathological correlates of late drug-eluting stent thrombosis: strut coverage as a marker of endothelialization. Circulation 115, 2435–2441. (doi:10.1161/ CIRCULATIONAHA.107.693739)
- Habib A, Finn AV. 2015 Endothelialization of drug eluting stents and its impact on dual anti-platelet therapy duration. *Pharmacol. Res.* 344, 1173–1178. (doi:10.1016/j.phrs.2014.12.003)
- Polyak B et al. 2016 Magnetic nanoparticlemediated targeting of cell therapy reduces in-stent stenosis in injured arteries. ACS Nano 10, 9559–9569. (doi:10.1021/acsnano.6b04912)
- Hsiao ST et al. 2016 Endothelial repair in stented arteries is accelerated by inhibition of Rhoassociated protein kinase. Cardiovasc. Res. 112, 689–701. (doi:10.1093/cvr/cvw210)
- Sprague EA, Tio F, Ahmed SH, Granada JF, Bailey SR. 2012 Impact of parallel micro-engineered stent grooves on endothelial cell migration, proliferation, and function: an *in vivo* correlation study of the healing response in the coronary swine model. *Circ. Cardiovasc. Interv.* 5, 499–507. (doi:10.1161/ CIRCINTERVENTIONS.111.967901)
- 14. Hamuro M, Palmaz JC, Sprague EA, Fuss C, Luo J. 2001 Influence of stent edge angle on endothelialization in an in vitro model. *J. Vasc. Interv. Radiol.* **12**, 607–611. (doi:10.1016/S1051-0443(07)61484-5)
- Aoki J et al. 2005 Endothelial progenitor cell capture by stents coated with antibody against CD34. J. Am. Coll. Cardiol. 45, 1574–1579. (doi:10.1016/j.jacc. 2005.01.048)
- Blindt R et al. 2006 A novel drug-eluting stent coated with an integrin-binding cyclic arg-gly-asp peptide inhibits neointimal hyperplasia by recruiting endothelial progenitor cells. J. Am. Coll. Cardiol. 47, 1786–1795. (doi:10.1016/j.jacc.2005.11.081)
- Nakazawa G et al. 2010 Anti-CD34 antibodies immobilized on the surface of sirolimus-eluting stents enhance stent endothelialization. *JACC Cardiovasc. Interv.* 3, 68–75. (doi:10.1016/j.jcin. 2009.09.015)
- Klomp M et al. 2011 1-year outcome of TRIAS HR (TRI-stent adjudication study—high risk of restenosis). JACC Cardiovasc. Interv. 4, 896—904. (doi:10.1016/j.jcin.2011.05.011)
- Hibbert B, Olsen S, O'Brien E. 2003 Involvement of progenitor cells in vascular repair. *Trends Cardiovasc. Med.* 13, 322–326. (doi:10.1016/j.tcm.2003.09.002)
- Hibbert B, Chen YX, O'Brien ER. 2004 c-kitimmunopositive vascular progenitor cells populate human coronary in-stent restenosis but not primary atherosclerotic lesions. *Am. J. Physiol. Heart Circ. Physiol.* 287, H518–H524. (doi:10.1152/ajpheart. 00002.2004)
- 21. Scott SM, Barth MG, Gaddy LR, Ahl ET. 1994 The role of circulating cells in the healing of vascular prostheses. *J. Vasc. Surg.* **19**, 585–593. (doi:10. 1016/S0741-5214(94)70030-3)

- Madonna R, De Caterina R. 2015 Circulating endothelial progenitor cells: do they live up to their name? *Vascul. Pharmacol.* 67–69, 2–5. (doi:10. 1016/j.vph.2015.02.018)
- Zhang M, Malik AB, Rehman J. 2014 Endothelial progenitor cells and vascular repair. *Curr. Opin. Hematol.* 21, 224. (doi:10.1097/MOH. 00000000000000001)
- 24. Isogai N, Kamiishi H, Chichibu S. 1988 Reendothelialization stages at the microvascular anastomosis. *Microsurgery* **9**, 87–92. (doi:10.1002/micr.1920090206)
- Itoh Y, Toriumi H, Yamada S, Hoshino H, Suzuki N. 2010 Resident endothelial cells surrounding damaged arterial endothelium reendothelialize the lesion. Arterioscler. Thromb. Vasc. Biol. 30, 1725–1732. (doi:10.1161/ATVBAHA.110.207365)
- Lindner V, Majack RA, Reidy MA. 1990 Basic fibroblast growth factor stimulates endothelial regrowth and proliferation in denuded arteries. J. Clin. Invest. 85, 2004—2008. (doi:10.1172/ JCI114665)
- Rogers C, Parikh S, Seifert P, Edelman BR. 1996 Endogenous cell seeding: remnant endothelium after stenting enhances vascular repair. *Circulation* 94, 2909–2914. (doi:10.1161/01.CIR.94.11.2909)
- 28. Cheneau E *et al.* 2003 Time course of stent endothelialization after intravascular radiation therapy in rabbit iliac arteries. *Circulation* **107**, 2153–2158. (doi:10.1161/01.CIR.0000062648.39025. 09)
- Van Belle E, Tio FO, Couffinhal T, Maillard L, Passeri J, Isner JM. 1997 Stent endothelialization: time course, impact of local catheter delivery, feasibility of recombinant protein administration, and response to cytokine expedition. *Circulation* 95, 438–448. (doi:10.1161/01.CIR.95.2.438)
- Tardy Y, Resnick N, Nagel T, Gimbrone MA, Dewey CF. 1997 Shear stress gradients remodel endothelial monolayers in vitro via a cell proliferationmigration-loss cycle. Arterioscler. Thromb. Vasc. Biol. 17, 3102–3106. (doi:10.1161/01.ATV.17.11.3102)
- 31. Hsu PP, Li S, Li YS, Usami S, Ratcliffe A, Wang X, Chien S. 2001 Effects of flow patterns on endothelial cell migration into a zone of mechanical denudation. *Biochem. Biophys. Res. Commun.* **285**, 751–759. (doi:10.1006/bbrc.2001.5221)
- Ostrowski MA, Huang NF, Walker TW, Verwijlen T, Poplawski C, Khoo AS, Cooke JP, Fuller GG, Dunn AR. 2014 Microvascular endothelial cells migrate upstream and align against the shear stress field created by impinging flow. *Biophys. J.* 106, 366–374. (doi:10.1016/j.bpj.2013.11.4502)
- Antoine EE, Cornat FP, Barakat Al. 2016 The stentable in vitro artery: an instrumented platform for endovascular device development and optimization. J. R. Soc. Interface 13, 20160834. (doi:10.1098/rsif.2016.0834)
- 34. Jiménez JM *et al.* 2014 Macro- and microscale variables regulate stent haemodynamics, fibrin deposition and thrombomodulin expression. *J. R. Soc. Interface* **11**, 20131079. (doi:10.1098/rsif.2013. 1079)

- Jiménez JM, Davies PF. 2009 Hemodynamically driven stent strut design. *Ann. Biomed. Eng.* 37, 1483–1494. (doi:10.1007/s10439-009-9719-9)
- 36. Jiménez JM, Davies PF. 2010 Design implications for endovascular stents and the endothelium. In *Hemodynamics and mechanobiology of endothelium*, pp. 291–312. Singapore: World scientific.
- Mejia J, Ruzzeh B, Mongrain R, Leask R, Bertrand OF. 2009 Evaluation of the effect of stent strut profile on shear stress distribution using statistical moments. *Biomed. Eng. Online* 8, 1–10. (doi:10. 1186/1475-925X-8-8)
- 38. Simon C, Palmaz JC, Sprague EA. 2000 Influence of topography on endothelialization of stents: clues for new designs. *J. Long Term Eff. Med. Implants.* **10**, 143–151.
- Kolandaivelu K, Swaminathan R, Gibson WJ, Kolachalama VB, Nguyen-Ehrenreich KL, Giddings VL, Coleman L, Wong GK, Edelman ER. 2011 Stent thrombogenicity early in high-risk interventional settings is driven by stent design and deployment and protected by polymer-drug coatings. *Circulation* 123, 1400—1409. (doi:10.1161/CIRCULATIONAHA. 110.003210)
- Chiastra C, Morlacchi S, Gallo D, Morbiducci U, Cardenes R, Larrabide I, Migliavacca F. 2013 Computational fluid dynamic simulations of imagebased stented coronary bifurcation models. J. R. Soc. Interface 10, 20130193. (doi:10.1098/rsif.2013.0193)
- 41. LaDisa JF. 2005 Alterations in wall shear stress predict sites of neointimal hyperplasia after stent implantation in rabbit iliac arteries. *AJP Heart Circ. Physiol.* **288**, H2465–H2475. (doi:10.1152/ajpheart. 01107.2004)
- Van der Heiden K, Gijsen FJH, Narracott A, Hsiao S, Halliday I, Gunn J, Wentzel JJ, Evans PC. 2013 The effects of stenting on shear stress: relevance to endothelial injury and repair. *Cardiovasc. Res.* 99, 269–275. (doi:10.1093/cvr/cvt090)
- Michalet X. 2010 Mean square displacement analysis of single-particle trajectories with localization error: Brownian motion in an isotropic medium. *Phys. Rev. E* 82, 041914. (doi:10.1103/ PhysRevE.82.041914)
- Reffay M, Parrini MC, Cochet-Escartin O, Ladoux B, Buguin A, Coscoy S, Amblard F, Camonis J, Silberzan P. 2014 Interplay of RhoA and mechanical forces in collective cell migration driven by leader cells. *Nat. Cell Biol.* 16, 217–223. (doi:10.1038/ncb2917)
- Doriot PA, Dorsaz PA, Dorsaz L, De Benedetti E, Chatelain P, Delafontaine P. 2000 In-vivo measurements of wall shear stress in human coronary arteries. *Coron. Artery Dis.* 11, 495–502. (doi:10.1097/00019501-200009000-00008)
- Saw TB, Jain S, Ladoux B, Lim CT. 2015
 Mechanobiology of collective cell migration. *Cell. Mol. Bioeng.* 8, 3–13. (doi:10.1007/s12195-014-0366-3)
- Ando J, Nomura H, Kamiya A. 1987 The effect of fluid shear stress on the migration and proliferation of cultured endothelial cells. *Microvasc. Res.* 33, 62–70. (doi:10.1016/0026-2862(87)90007-0)

- 48. Virmani R *et al.* 2004 Localized hypersensitivity and late coronary thrombosis secondary to a sirolimus-eluting stent. *Circulation* **109**, 701–705. (doi:10. 1161/01.CIR.0000116202.41966.D4)
- Guagliumi G, Farb A, Musumeci G, Valsecchi O, Tespili M, Motta T, Virmani R. 2003 Sirolimuseluting stent implanted in human coronary artery for 16 months. *Circulation* 107, 1340–1341. (doi:10. 1161/01.CIR.0000062700.42060.6F)
- Sousa JE et al. 2004 Vascular healing 4 years after the implantation of sirolimus-eluting stent in humans. Circulation 110, e5—e6. (doi:10.1161/01. CIR.0000134307.00204.B3)
- 51. Yau JW, Teoh H, Verma S. 2015 Endothelial cell control of thrombosis. *BMC Cardiovasc. Disord.* **15**, 130. (doi:10.1186/s12872-015-0124-z)
- Achneck HE, Sileshi B, Parikh A, Milano CA, Welsby IJ, Lawson JH. 2010 Pathophysiology of bleeding and clotting in the cardiac surgery patient. Circulation 122, 2068–2077. (doi:10.1161/ CIRCULATIONAHA.110.936773)
- 53. Palta S, Saroa R, Palta A. 2014 Overview of the coagulation system. *Indian J. Anaesth.* **58**, 515. (doi:10.4103/0019-5049.144643)
- Foin N et al. 2014 Impact of stent strut design in metallic stents and biodegradable scaffolds. Int. J. Cardiol. 177, 800–808. (doi:10.1016/j.ijcard. 2014.09.143)
- Zhu T, Gao W, Fang D, Liu Z, Wu G, Zhou M, Wan M, Mao C. 2020 Bifunctional polymer brush-grafted coronary stent for anticoagulation and endothelialization. *Mater. Sci. Eng. C* 120, 111725. (doi:10.1016/j.msec.2020.111725)
- Bae IH, Jeong MH, Lim KS, Park DS, Shim JW, Park JK, Oh KH, Jin MR, Sim DS. 2018 Novel polymer-free everolimus-eluting stent fabricated using femtosecond laser improves re-endothelialization and anti-inflammation. *Sci. Rep.* 8, 7383. (doi:10. 1038/s41598-018-25629-9)

- 57. Papafaklis MI, Chatzizisis YS, Naka KK, Giannoglou GD, Michalis LK. 2012 Drug-eluting stent restenosis: effect of drug type, release kinetics, hemodynamics and coating strategy. *Pharmacol. Ther.* **134**, 43–53. (doi:10.1016/j.pharmthera.2011.12.006)
- Sakamoto A, Jinnouchi H, Torii S, Virmani R, Finn AV. 2018 Understanding the impact of stent and scaffold material and strut design on coronary artery thrombosis from the basic and clinical points of view. *Bioengineering* 5, 71. (doi:10.3390/ bioengineering5030071)
- Palmaz JC, Bailey S, Marton D, Sprague E. 2002 Influence of stent design and material composition on procedure outcome. *J. Vasc. Surg.* 36, 1031–1039. (doi:10.1067/mva.2002.129113)
- Yamamoto T *et al.* 1996 Blood velocity profiles in the human renal artery by Doppler ultrasound and their relationship to atherosderosis. *Arteriosder. Thromb. Vasc. Biol.* 16, 172–177. (doi:10.1161/01.ATV. 16.1.172)
- Chiu J-J, Chien S. 2011 Effects of disturbed flow on vascular endothelium: pathophysiological basis and clinical perspectives. *Physiol. Rev.* 91, 327–387. (doi:10.1152/physrev.00047.2009)
- 62. Davies PF. 1995 Flow-mediated endothelial mechanotransduction. *Physiol. Rev.* **75**, 519–560. (doi:10.1152/physrev.1995.75.3.519)
- 63. Etienne-Manneville S, Hall A. 2002 Rho GTPases in cell biology. *Nature* **420**, 629–635. (doi:10.1038/nature01148)
- Ridley AJ. 2001 Rho GTPases and cell migration. J. Cell Sci. 114, 2713–2722. (doi:10.1242/jcs.114.15. 2713)
- Liu B, Lu S, Hu Y, Liao X, Ouyang M, Wang Y. 2015 RhoA and membrane fluidity mediates the spatially polarized Src/FAK activation in response to shear stress. Sci. Rep. 4, 7008. (doi:10.1038/srep07008)
- 66. Wojciak-Stothard B, Ridley AJ. 2003 Shear stress—induced endothelial cell polarization is mediated by

- Rho and Rac but not Cdc42 or PI 3-kinases. *J. Cell Biol.* **161**, 429–439. (doi:10.1083/jcb.200210135)
- DePaola N, Gimbrone MA, Davies PF, Dewey CF.
 1992 Vascular endothelium responds to fluid shear stress gradients. *Arterioscler. Thromb. J. Vasc. Biol.* 12, 1254–1257. (doi:10.1161/01.ATV.12.11.1254)
- Udan RS, Vadakkan TJ, Dickinson ME. 2013 Dynamic responses of endothelial cells to changes in blood flow during vascular remodeling of the mouse yolk sac. *Development* 140, 4041–4050. (doi:10.1242/ dev.096255)
- Yamaguchi N, Mizutani T, Kawabata K, Haga H. 2015 Leader cells regulate collective cell migration via Rac activation in the downstream signaling of integrin β1 and PI3 K. Sci. Rep. 5, 7656. (doi:10.1038/srep07656)
- Omelchenko T, Vasiliev JM, Gelfand IM, Feder HH, Bonder EM. 2003 Rho-dependent formation of epithelial 'leader' cells during wound healing. *Proc. Natl Acad. Sci.* 100, 10 788–10 793. (doi:10.1073/ pnas.1834401100)
- Moldovan L, Moldovan NI, Sohn RH, Parikh SA, Goldschmidt-Clermont PJ. 2000 Redox changes of cultured endothelial cells and actin dynamics. *Circ. Res.* 86, 549–557. (doi:10.1161/01.RES.86.5.549)
- Civelek M, Manduchi E, Riley RJ, Stoeckert CJ, Davies PF. 2011 Coronary artery endothelial transcriptome in vivo. Circ. Cardiovasc. Genet. 4, 243–252. (doi:10. 1161/CIRCGENETICS.110.958926)
- 73. Gojova A, Barakat Al. 2005 Vascular endothelial wound closure under shear stress: role of membrane fluidity and flow-sensitive ion channels. *J. Appl. Physiol.* **98**, 2355–2362. (doi:10.1152/japplphysiol.01136.2004)
- Frangos JA, Huang TY, Clark CB. 1996 Steady shear and step changes in shear stimulate endothelium via independent mechanisms—superposition of transient and sustained nitric oxide production. *Biochem. Biophys. Res. Commun.* 224, 660–665. (doi:10.1006/bbrc.1996.1081)